

# Establishment, validation and discussions of a three dimensional wave-induced current model

Mingxiao Xie \*

Tianjin Research Institute for Water Transport Engineering, M.O.T., Tianjin 300456, China  
College of Civil Engineering, Tianjin University, Tianjin 300072, China

## ARTICLE INFO

### Article history:

Received 8 June 2010

Received in revised form 18 March 2011

Accepted 27 March 2011

Available online 1 April 2011

### Keywords:

Three dimensional wave-induced current model

Surface roller evolution model

Wave turbulent mixing

Model validation

Sensitivity analysis

## ABSTRACT

A three-dimensional numerical model was established to simulate the wave-induced currents. The depth-varying residual momentum, surface roller, wave horizontal and vertical turbulent mixing effects were incorporated as major driving forces. A surface roller evolution model considering the energy transfer, roller density and bottom slope dissipation was developed. The expression of the wave-induced horizontal turbulent mixing coefficient proposed by Larson and Kraus (1991) was extended to three-dimensional form. Plenty of experimental cases were used to validate the established model covering the wave setup, undertow, longshore currents and rip currents. Validation results showed the model could reasonably describe the main characteristics of different wave-induced current phenomena. The incorporation of surface roller for breaking waves should not be neglected in the modeling of surfzone hydrodynamics. The wave-induced turbulent mixing affects the structures of wave-induced current either in horizontal or in vertical directions. Sensitivity analysis of the major calibration parameters in the established model was made and their ranges were evaluated.

© 2011 Elsevier Ltd. All rights reserved.

## 1. Introduction

In coastal regions, the wave-induced currents generated in the nearshore can be very intense, and they are directly responsible for sediment transport processes and morphological evolutions. Therefore, the accurate prediction of these currents is essential for coastal engineering applications. Under different wave/topography conditions, the wave-induced currents present variable features e.g. the wave setup/down, undertow, longshore currents, and rip currents. In natural coastal environments, these currents usually superpose on each other, and form an extremely complex nearshore circulation system.

The historical research works on the wave-induced currents mainly emphasized their horizontal distribution features, but the explorations of the vertical structure are insufficient. Commonly, the gradient of wave-induced period-averaged residual momentum flux (taken as “residual momentum” for abbreviation) is recognized as the primary driving force of the wave-induced currents. As for the horizontal two-dimensional (2DH) modeling, the concept of radiation stresses proposed by Longuet-Higgins and Stewart (1964) is widely applied. However, the radiation stresses are depth-averaged values, and they cannot describe the

vertical profile of the residual momentum, hence they are insufficient for the investigations of undertow. In recent years, based on different approaches, a number of formulations have been derived to describe the depth-varying residual momentum e.g. the generalized Lagrangian mean (GLM) method (Ardhuin et al., 2008; Lin and Zhang, 2004), vertical mapping method (Mellor, 2003, 2005), vortices force method (McWilliams et al., 2004) and Eulerian mean method (Xia et al., 2004). Mostly, the linear wave assumption is used in their derivations. Moreover, aiming at the shallow water waves, nonlinear wave theories (e.g. Stokes 2nd; Cnoidal) were also reported (Wang et al., 2008; Svendsen et al., 2003). Based on the latest achievements, some researchers consequently incorporated the above formulations into 3D hydrodynamic models. Xie et al. (2008) adopted the Xia et al. (2004) formulation into the POM model; Warner et al. (2008) introduced the Mellor (2005) expression into the ROMS model, and Wu and Zhang (2009) applied the Lin and Zhang (2004) formulation into the ELCIRC model.

Other than the residual momentum, some other factors also contribute to the structure of wave-induced currents. A great number of laboratory experiments and field observations proved that rather than at the breaking point, the wave setup begins well inside the surfzone, and the speed of the longshore current also reach its peak at a notable distance shoreward of incipient breaking. Thereby, Svendsen (1984a,b) developed the concept of surface roller, and believed that the aerated region on the breaking wave crest

\* Address: Tianjin Research Institute for Water Transport Engineering, M.O.T., Tianjin 300456, China. Tel.: +86 22 59812345.

E-mail address: [crabsaver@163.com](mailto:crabsaver@163.com)

could bring in additional momentum terms. Duncan (1981), Engelund (1981) and Okayasu et al. (1990) respectively formulated relevant empirical expressions to characterize the behavior of surface rollers. Dally and Brown (1995) firstly established an energy balance model to describe the roller evolution. Tajima and Madsen (2002) and Goda (2006) further improved the Dally-Brown model to account for different breaker types and multiple bed slopes. However, the Tajima-Madsen and Goda model neglected the density difference between the seawater and the rollers, which seems unrealistic for the natural situations.

The orbital motions of water wave particles bring in additional turbulent mixings which could affect the flow structure (Putrevu and Svendsen, 1999). Similar to the modeling of tidal currents, at present the concept of mixing coefficients is applied to parameterize the wave-induced turbulence, and these coefficients are related to wave parameters e.g. the wave height, wave period and water depth (Larson and Kraus, 1991; Wang, 1984).

In this paper, a hydrodynamic model is developed to simulate the 3D structure of the wave-induced currents, and a number of representative experimental cases are used to test the model behavior. Finally, some discussions on the model parameters are also given.

## 2. Model description

### 2.1. Hydrodynamic model

The governing equations of the hydrodynamic model follow the Reynolds form simplified from the original Navier–Stokes equations (see Eqs. (1)–(4)). As for the modeling of wave-induced currents, the residual momentum, surface roller and turbulent mixings are included as the major driving forces. Cartesian coordinates are used in the horizontal and the terrain-following sigma coordinate is used in the vertical.

$$\frac{\partial \eta}{\partial t} + \frac{\partial UD}{\partial x} + \frac{\partial VD}{\partial y} + \frac{\partial \omega}{\partial \sigma} = 0 \quad (1)$$

$$\begin{aligned} & \frac{\partial UD}{\partial t} + \frac{\partial U^2 D}{\partial x} + \frac{\partial UVD}{\partial y} + \frac{\partial \omega U}{\partial \sigma} \\ & = -gD \frac{\partial \eta}{\partial x} + \frac{\partial}{\partial x} \left( 2A_{Mc} D \frac{\partial U}{\partial x} \right) + \frac{\partial}{\partial y} \left[ A_{Mc} D \left( \frac{\partial U}{\partial y} + \frac{\partial V}{\partial x} \right) \right] \\ & + \frac{\partial}{\partial \sigma} \left( \frac{K_{Mc}}{D} \frac{\partial U}{\partial \sigma} \right) - \frac{D}{\rho} \left( \frac{\partial M_{xx}}{\partial x} + \frac{\partial M_{xy}}{\partial y} \right) - \frac{D}{\rho} \left( \frac{\partial R_{xx}}{\partial x} + \frac{\partial R_{xy}}{\partial y} \right) \end{aligned} \quad (2)$$

$$\begin{aligned} & \frac{\partial VD}{\partial t} + \frac{\partial V^2 D}{\partial y} + \frac{\partial VUD}{\partial x} + \frac{\partial \omega V}{\partial \sigma} \\ & = -gD \frac{\partial \eta}{\partial y} + \frac{\partial}{\partial y} \left( 2A_{Mc} D \frac{\partial V}{\partial y} \right) + \frac{\partial}{\partial x} \left[ A_{Mc} D \left( \frac{\partial V}{\partial x} + \frac{\partial U}{\partial y} \right) \right] \\ & + \frac{\partial}{\partial \sigma} \left( \frac{K_{Mc}}{D} \frac{\partial V}{\partial \sigma} \right) - \frac{D}{\rho} \left( \frac{\partial M_{yx}}{\partial x} + \frac{\partial M_{yy}}{\partial y} \right) - \frac{D}{\rho} \left( \frac{\partial R_{yx}}{\partial x} + \frac{\partial R_{yy}}{\partial y} \right) \end{aligned} \quad (3)$$

$$-\frac{1}{\rho} \frac{\partial p}{\partial \sigma} - gD = 0 \quad (4)$$

where the vertical sigma coordinate  $\sigma = (z - \eta)/D$  ranges from  $\sigma = -1$  at the bottom to  $\sigma = 0$  at the surface;  $t$  is time;  $x$  and  $y$  are horizontal coordinates, respectively;  $\eta$  is the free surface;  $U$  and  $V$  are velocity components for  $x$  and  $y$  directions, respectively;  $\omega$  is the velocity component under  $\sigma$  coordinate;  $D$  is the water depth;  $g$  is gravity;  $p$  is pressure;  $M$  is the depth-varying residual momentum;  $R$  is the depth-varying roller momentum;  $K_{Mc}$  and  $A_{Mc}$  are vertical and horizontal mixing coefficients combining waves and currents, respectively;  $\rho$  is the seawater density.

### 2.2. Wave-induced residual momentum

The formulation proposed by Lin and Zhang (2004) is applied for the vertical distribution of wave-induced residual momentum. The derivation methodology for the Lin-Zhang formulation is based on vertical expression of the Navier–Stokes equations. The viscous term is neglected, and the water density is assumed as constant. Using linear wave theory and the GLM method, the depth-dependent residual pressure is expressed, which is a generalized extension of the Longuet-Higgins form. Readers can refer to Lin and Zhang (2004) for the detailed derivations. The ultimate expression for the wave-induced residual momentum follows Eq. (5).

$$\begin{aligned} M_{ij}(\sigma) = & En \frac{k_x k_y}{k^2} \left( \frac{2k \cosh^2 k(1+\sigma)D}{kD + \sinh kD \cosh kD} \right) \\ & + \delta_{ij} \left[ \frac{Ek}{2 \sinh^2 kD} \sinh 2k(1+\sigma)D - \frac{2Ek}{\sinh 2kD} \sinh^2 k(1+\sigma)D \right] \end{aligned} \quad (5)$$

where  $E$  is the wave energy;  $n$  is the wave energy transfer rate;  $k$  is the wave number;  $\sigma_w$  is the wave annular frequent;  $T$  is the wave period;  $\delta$  is the Kronecker symbol;  $i$  and  $j$  represent the  $x, y$  direction, respectively.

### 2.3. Bottom shear stress

The wave-current combined bottom shear stress  $\tau_{cw}$  is determined as formulated by Soulsby et al. (1993), see Eq. (6).

$$\frac{\tau_{cw}}{\tau_c + \tau_w} = \frac{\tau_c}{\tau_c + \tau_w} \left[ 1 + B \left( \frac{\tau_c}{\tau_c + \tau_w} \right)^P \left( \frac{\tau_w}{\tau_c + \tau_w} \right)^Q \right] \quad (6)$$

where  $\tau_c = \rho C_D u_c^2$  is the bed shear stress by current only,  $C_D = \left( \frac{1}{\kappa} \ln(h + z_b)/z_0 \right)^{-2}$  is the drag coefficient, where  $\kappa = 0.4$  is the von Karman constant;  $h$  is the bed elevation;  $z_b$  is the elevation of the grid point nearest the bottom;  $z_0$  is the roughness height;  $u_c$  is the current velocity at the grid point nearest the bed;  $\tau_w = \frac{1}{2} \rho f_w u_w^2$  is the shear stress due to waves only;  $u_w = \frac{H\pi}{T \sinh(kD)}$  is the near-bottom wave orbital velocity;  $f_w$  is the wave friction factor following Swart (1974);  $B, P, Q$  are empirical coefficients, respectively. The value of coefficient  $B$  is given by Eq. (7)

$$B = (b_1 + b_2 |\cos \phi|^J) + (b_3 + b_4 |\cos \phi|^J) \log(f_w/C_D) \quad (7)$$

with analogous expressions for  $P$  and  $Q$ . The values of parameters  $(b, p, q)_{1-4}$  and  $J$  follow those suggested in Soulsby et al. (1993).

### 2.4. Wave model

The combined refraction/diffraction wave model (REF/DIF) is used as the wave driver for simulating monochromatic incident waves. It solves the parabolic mild-slope equation initially developed by Kirby et al. (1994), and involves many processes e.g. shoaling, refraction, energy dissipation, and irregular bottom bathymetry. Wave-current interactions can also be considered.

### 2.5. Turbulence mixing

At present, the turbulence theory considering the mutual interactions of waves and currents is still not well established. Therefore, similar to the approach applied by Xia et al. (2004), in this paper the turbulent mixing coefficient is linearly added using the current turbulent mixing coefficient and the wave turbulent mixing coefficient, see Eq. (8) and (9).

$$A_{Mc}(\sigma) = A_M(\sigma) + A_W(\sigma) \quad (8)$$

$$K_{Mc}(\sigma) = K_M(\sigma) + K_W(\sigma) \quad (9)$$

where  $A$  and  $K$  represent horizontal and vertical turbulent mixing coefficients, respectively, and the subscripts  $M$  and  $W$  represent current and waves, respectively.

### 2.5.1. Horizontal mixing

The horizontal mixing coefficient  $A_M$  for currents only is given by Smagorinsky (1963)

$$A_M = C_s^2 \Delta x \Delta y \left[ \left( \frac{\partial U}{\partial x} \right)^2 + \left( \frac{\partial V}{\partial y} \right)^2 + \frac{1}{2} \left( \frac{\partial U}{\partial y} + \frac{\partial V}{\partial x} \right)^2 \right]^{\frac{1}{2}} \quad (10)$$

where  $\Delta x$  and  $\Delta y$  are horizontal grid steps;  $C_s$  is an empirical factor, commonly in the range of 0.1–0.2.

Some formulations have been proposed to describe the wave-induced horizontal turbulent mixing e.g. Longuet-Higgins and Stewart (1964), Battjes (1975) and Larson and Kraus (1991). Through comparisons, Goda (2006) pointed out that the Larson–Kraus expression has best performance when modeling the long-shore current, see Eq. (11)

$$A_W = \lambda u_{\max} H \quad (11)$$

where  $\lambda$  is a nondimensional coefficient having a value around 0.3 to 0.5;  $u_{\max}$  is the maximum wave orbital velocity at the bottom. In fact, the excursion amplitude of wave particles varies between vertical layers, implying that the value of the mixing coefficient is non-uniform along the vertical profile. Therefore, in this paper we extend the Larson–Kraus formulation to the 3D form applying the linear wave theory, and substitute  $u_{\max}$  with  $u_{\max}(\sigma)$ , which yields:

$$A_W(\sigma) = \frac{2\lambda H^2 \cosh((1 + \sigma)kD)}{T \sinh(kD)} \quad (12)$$

### 2.5.2. Vertical mixing

The current-induced vertical mixing coefficient  $K_M$  is solved using a closure model proposed by Mellor and Yamada (1982). Investigations on the wave vertical turbulence are rare. The former Soviet Union scholars Башкиров and Жуковен have derived an expression for the depth varying vertical mixing coefficient  $K_M$  using linear wave theory, which was introduced by Wang (1984), and it yields

$$K_W(\sigma) = \frac{bgTH \cosh(k(1 + \sigma)D)}{4\pi \cosh kD} \quad (13)$$

where  $b$  is a calibration coefficient, and its value is in the order of  $O(10^{-3})$ .

### 2.6. Roller evolution model

The basic idea of the surface roller evolution model originates from the energy balance equation proposed by Dally and Brown (1995), see Eq. (14).

$$\frac{dE}{dx} + \frac{d}{dx} \left( \frac{1}{2} \rho_R \beta_c^2 C^2 \frac{A_R}{T} \right) = -\rho_R g \beta_D \frac{A_R}{T} \quad (14)$$

where  $\rho_R$  is the roller density;  $A_R$  is the roller area;  $C$  is the celerity;  $\beta_c$  and  $\beta_D$  are empirical coefficients. Some subsequent works have been made to improve the Dally–Brown equation. Tajima and Madsen (2002) developed it for an arbitrary direction, and brought in an additional parameter called the roller energy transfer factor to account for different breaker types. Goda (2006) further considered the contribution of bottom dissipation, see Eq. (15).

$$\nabla(EC_g \vec{n}) + \alpha \nabla(E_R C \vec{n}) = -\frac{K_R C}{D} E_R \quad (15)$$

where  $C_g = Cn$  is the wave group celerity;  $\alpha$  is the roller energy transfer factor taking a value between 0.0 and 1.0;  $E_R = \frac{\rho_R A_R C}{2T}$  is the

roller energy;  $\vec{n} = n(\cos \theta, \sin \theta)$  is the wave direction vector;  $K_R = \frac{3}{8}(0.3 + 2.4s)$ , and  $s$  is the bed slope. However, different from the original Dally–Brown form, the Goda model actually implied  $\rho_R = \rho$ , which is not practical for the realistic situations. In fact, when waves break and the crests contain a large amount of air, its density should be smaller than the seawater. Considering this, in this paper we integrated the ideas of three models (Dally–Brown model, Tajima–Madsen model and Goda model), and derived a new energy balance equation incorporating the roller transfer factor, roller density and the bottom dissipation, which yields:

$$\nabla(EC_g \vec{n}) + \alpha \nabla \left( \frac{\rho_R A_R}{2T} C^2 \vec{n} \right) = -\frac{K_R}{h} \frac{\rho_R A_R}{2T} C^2 \quad (16)$$

If the wave parameters are given, Eq. (16) could be solved using an iteration algorithm from the breaking point to the shoreline with an offshore boundary condition  $A_R = 0$ . The vertical profile of the roller momentum is expressed as an exponential function proposed by Haas and Warner (2009), see Eq. (17). Note that because the depth integral of  $R_z$  should be unity, it should be pre-normalized to  $R_{zn}$  following Eq. (18).

$$R_z(\sigma) = 1 - \tanh \left( \frac{2\sigma h}{H} \right)^4 \quad (17)$$

$$R_{zn}(\sigma) = R_z(\sigma) / \int_{-1}^0 R_z(\sigma) d\sigma \quad (18)$$

Once  $A_R(\sigma)$  is solved,  $E_R(\sigma)$  could be calculated explicitly. The corresponding stresses in the governing equations caused by the roller could be determined.

$$R_{xx}(\sigma) = 2E_R(\sigma) \cos^2 \theta R_{zn}(\sigma) \quad (19)$$

$$R_{xy}(\sigma) = R_{yx}(\sigma) = 2E_R(\sigma) \sin \theta \cos \theta R_{zn}(\sigma) \quad (20)$$

$$R_{yy}(\sigma) = 2E_R(\sigma) \sin^2 \theta R_{zn}(\sigma) \quad (21)$$

### 2.7. Solution technique

A finite different method and time-splitting technique are applied to solve the governing equations. The horizontal terms are treated explicitly, and the vertical terms are treated implicitly using a double-sweep scheme. The staggered C-grid system is used. The wave set-up near the shoreline would induce an inundation. A variety of approaches on the inundation scheme have been reported in literature. In this paper, the inundation scheme follows the OGCM approach proposed by Oey (2006).

### 3. Model validation

Once a numerical modelling system is established, observation datasets need to be used to test its behavior. Therefore, the validation process is performed in the later sections, and a number of experimental cases covering different dimensions e.g. the wave setup (1D), undertow (2DV), longshore currents (quasi-3D), rip currents (3D) are used.

As for error estimation, the root-mean square error  $RMS$  and the correlation coefficient  $COR$  are applied; the former reflects the deviation between the measured and simulated values, and the latter represents the linear correlation of the two datasets. Note that the space locations of the measured and simulated variables may not coincide, hence for each valid measurement at location  $z_i$  (or  $x_i$ ), the corresponding model value is extracted from the model results using linear interpolation between the model steps before and after  $z_i$  (or  $x_i$ ). The calculation formulations for both model skill statistics are:

$$RMS = \sqrt{\frac{1}{N} \sum_{I=1}^N (me_I - mo_I)^2} \quad (22)$$

$$COR = \frac{\sum_{I=1}^N (me_I - \overline{me})(mo_I - \overline{mo})}{\sqrt{\sum_{I=1}^N (me_I - \overline{me})^2 \sum_{I=1}^N (mo_I - \overline{mo})^2}} \quad (23)$$

where  $N$  is the total number of measurement points;  $I$  is the index of a measurement value;  $me$  is the measurement value;  $mo$  is the modeled value;  $\overline{me} = \frac{1}{N} \sum_{I=1}^N me_I$  and  $\overline{mo} = \frac{1}{N} \sum_{I=1}^N mo_I$  represent the algebraic mean of the measured and modeled values, respectively.

### 3.1. Undertow

#### 3.1.1. Ting–Kirby experiment

Ting and Kirby (1994) studied the undertow within the surfzone using a wave tank for both plungers and spillers. The bed slope is set to 1:35, and the deep water depth is 0.40 m. Two regular wave cases are used to test the numerical model. The incident wave condition for the plunger case is  $H_0 = 0.089$  m,  $T = 5.0$  s; and for the spiller case  $H_0 = 0.127$  m,  $T = 2.0$  s. The input parameters in the numerical models are listed in Table 1.

For a vertical two-dimensional (2DV) undertow case, the depth integral of modeled velocity profiles from Eq. (1)–(4) should be zero since they are Lagrangian, but the observed velocities are under the Eulerian frame. As a result, the Stokes drift should be removed from the simulated velocities before comparisons. The conversion of these two reference frames is shown as:

$$(U, V)^E = (U, V)^L - (U, V)^S \quad (24)$$

where the superscripts  $E$ ,  $L$ , and  $S$  represent Eulerian, Lagrangian and Stokes velocities, respectively. The Stokes velocities are computed as:

$$U^S = \frac{2k_x}{c} \frac{\cosh 2kD(1 + \sigma)}{\sinh(2kD)} \left( \frac{E}{\rho} + \frac{DgA_R}{L} \right) \quad (25)$$

$$V^S = \frac{2k_y}{c} \frac{\cosh 2kD(1 + \sigma)}{\sinh(2kD)} \left( \frac{E}{\rho} + \frac{DgA_R}{L} \right) \quad (26)$$

The Stokes drifts are subtracted from the Lagrangian velocities to maintain a consistent Eulerian reference frame for the output. This frame conversion applies for all the model/data comparisons below. It should be emphasized that due to the strong nonlinearity, the wave models using linear theory may not describe the breakers precisely, and could underestimate the breaker height for 20%–60% (Svendsen et al., 2003). Therefore, the fitting of the measured wave heights could avoid the shortcomings by a wave model. Comparisons between the simulated/fitted and observed wave heights, wave setups and velocity profiles for both plunger and spiller cases are shown in Fig. 1 and Fig. 2, respectively. As for the wave setups, the model grasped their major distribution trends, leading to a  $COR = 0.92$  (see Fig. 1b) for the plunger case and  $COR = 0.83$  for the spiller case (see Fig. 2b). However, the model overestimated the maximum setup and setdown values for both cases, while the simulated onshore variations of the wave setups are also more

intense than that observed. The  $RMS$  error for the wave setup reaches 0.007 m for the plunger case and 0.008 m for the spiller case, which are in the same order of the measurement values, and the maximum errors occur near the breaking points. These errors could lead to exaggerated pressure gradients, which bring in unavoidable errors to the following undertow structures.

For the velocities, the  $RMS$  errors are in the range of 0.02–0.06 m/s. The errors between the observed and simulated velocities are larger near the breaking points for both cases, where the correlations  $COR$  are in the range of  $-0.49$  to  $0.30$ . The primary reason is that the wave setups are poorly predicted near the breaking points, which makes the pressure balance inappropriate. Additionally, it should be stressed that the observed data show that the peak values of undertow appear at the middle layer not far from the wave trough, but the maximum undertow of the simulated values are near the bottom. Other than the pressure gradients caused by the wave setup, this phenomenon seems more related to the natural differences between the linear wave theory and the cnoidal breakers especially near the breaking point where the nonlinearity is significant. Away from the breaking point, the errors between the two datasets are smaller, and the corresponding  $COR$  ranges from 0.73 to 0.92.

The plunger case is selected as an example to visualize the undertow structure (see Fig. 3). Within the surfzone, the currents in the upper water column flow to the shoreline, which induces a returning flow (undertow) pointing to the offshore. After the Stokes conversion, the speeds of shoreward flow are smaller than the undertow velocities in the surfzone. This feature is similar with that described by Svendsen (1984b) and Haas and Warner (2009).

#### 3.1.2. CROSSTEX Experiment

Scott et al. (2004) investigated the undertow structure on a barred beach through a large wave flume CROSSTEX. The flume is 104 m long, 3.7 m wide, and 4.6 m deep, the experimental condition is somewhat close to the realistic coastal environment. The bathymetry, observed wave heights and locations of observation gauges are shown in Fig. 4, and the period of incident waves is 4.0 s. In this paper the regular wave case is used, and the input parameters are listed in Table 1. The REF/DIF model is applied as the wave solver, and the comparison of observed and simulated wave heights is shown in Fig. 5a. For sections offshore to section P6, the modeled wave heights agree well with the observed data. However, the agreement is not satisfactory for locations around section P7, and this may bring inevitable errors for the wave setup and undertow structures in this area.

The comparisons of wave setup and velocity structures are shown from Fig. 5b to Fig. 5i. For the wave setup, the  $RMS$  error is 0.006 m, and  $COR$  is 0.96. This error is smaller compared to the Ting and Kirby cases.

The correlations for the undertow profiles for P1–P6 are from  $COR = 0.79$  to  $COR = 0.99$ . Note that for section P4 where the depth is shallowest, the undertow is underestimated with  $RMS = 0.14$  m/s. For section P7 (see Fig. 5i), although the  $RMS$  error is not as significant (0.07 m/s) compared to other sections, the curvature of the simulated undertow profile is opposite to that observed only with

**Table 1**  
Input parameters in the numerical model for different experimental cases.

Experiment	Spacing (m)	$\sigma$ layers	Time step (s)	$b$	$\alpha$	$\rho_R$ (kg/m <sup>3</sup> )	$\lambda$
Ting–Kirby plunger	0.1	11	0.015	0.001	0.60	900	0.20
Ting–Kirby spiller	0.1	11	0.015	0.001	0.50	900	0.20
CROSSTEX	0.4	11	0.04	0.001	0.50	800	0.20
Visser 4#	0.2	6	0.03	0.001	0.40	900	0.40
Visser 6#	0.2	6	0.03	0.001	0.30	900	0.50
Borthwick–Foote	0.1	18	0.01	0.001	0.40	800	0.40

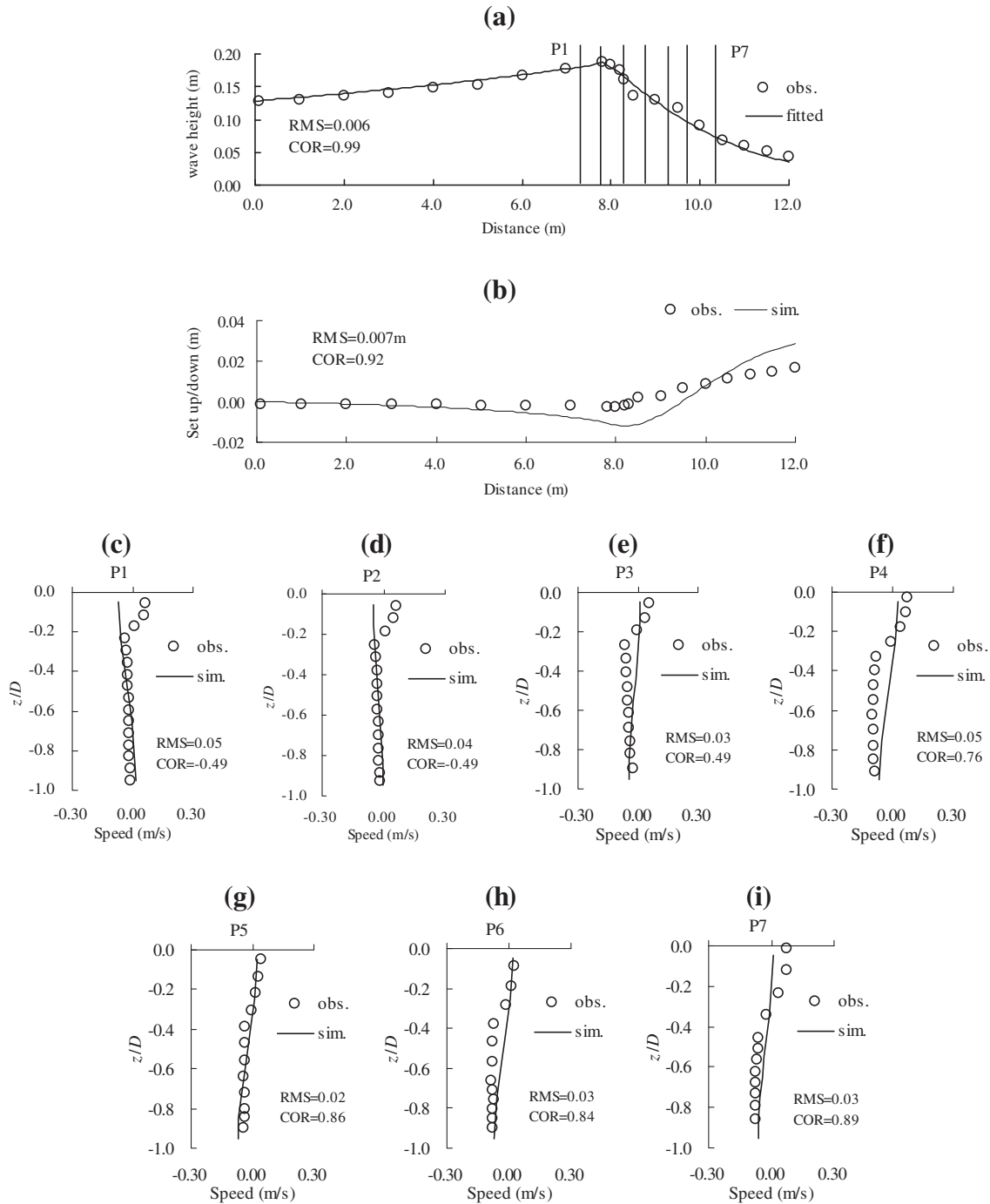


Fig. 1. Comparisons between the simulated/fitted and observed values for the Ting-Kirby plunger case. (a) wave height, (b) wave setup, (c)–(i) velocities.  $z/D$  is relative depth.

$COR = 0.13$ . That is because the wave height prediction is poor near this section, hence may lead to an unrealistic wave setup and velocity structures. Nevertheless, the overall trends of both wave setup and undertow structures are grasped.

### 3.2. Longshore currents

Visser (1991) investigated the characteristics of longshore currents in the laboratory. The bed slope is set to 1:20, and the deep water depth is 0.35 m. The cases for Exp. No. 4# (plunger) and Exp. No. 6# (plunger/spiller) are used in this paper. The incident

wave condition for case 4# is  $H_0 = 0.085$  m,  $T = 1.02$  s,  $\theta = 15.4^\circ$ ; and the condition for case 6# is  $H_0 = 0.06$  m,  $T = 0.7$  s,  $\theta = 15.4^\circ$ . The input parameters in the numerical model are listed in Table 1.

Similar to the Ting-Kirby cases, the wave heights are fitted to the measurements with a satisfactory precision ( $RMS < 0.005$  m,  $COR = 0.99$ ). Comparisons between the simulated and observed depth-averaged longshore current speeds for both cases are given in Fig. 6. The results show that the modeled longshore currents agree well with the observed data in both peak values and the horizontal variations. The RMS errors of the longshore current speeds are less than 0.04 m/s, and the correlations  $COR$  are larger than 0.97.

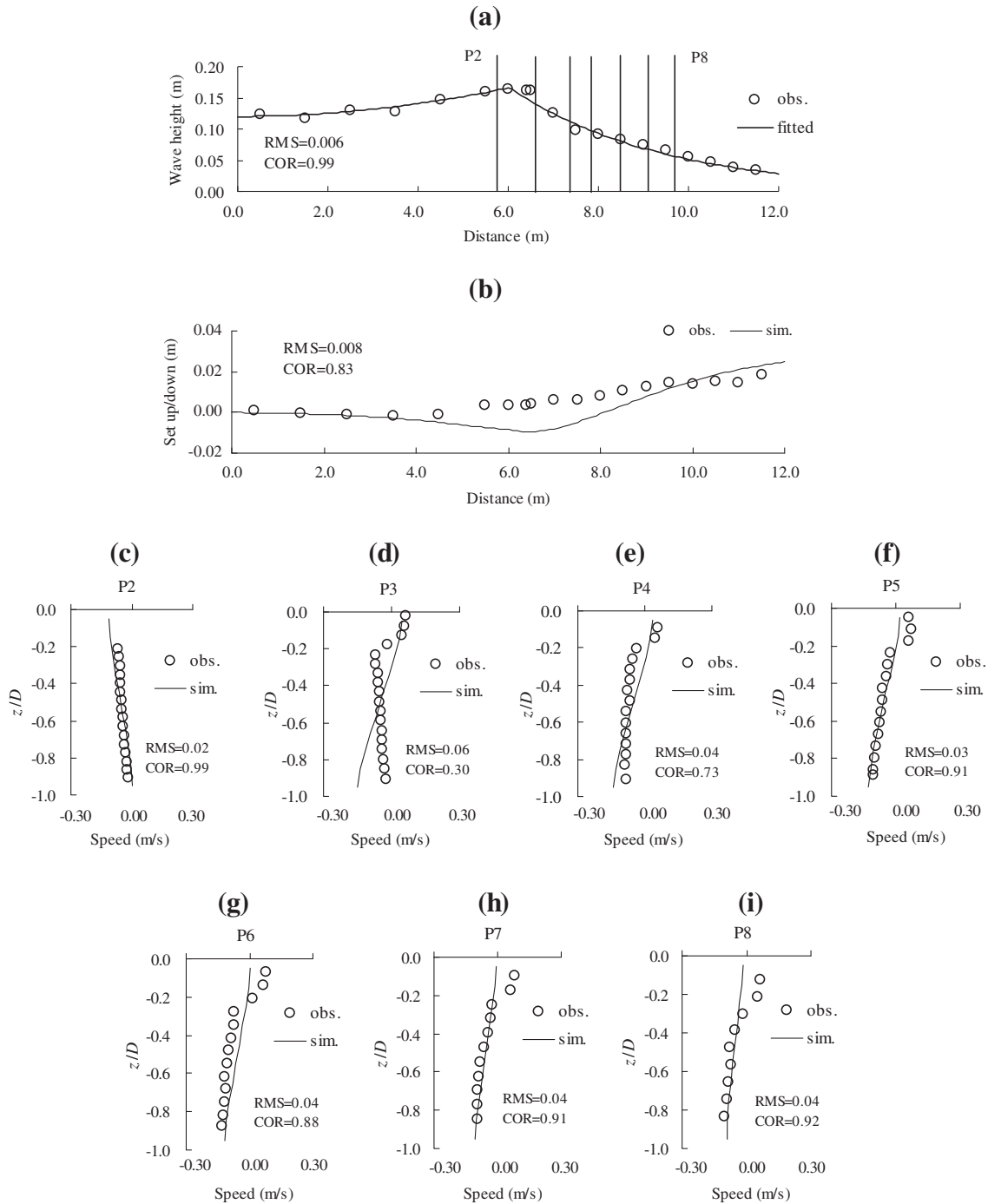


Fig. 2. Comparisons between the simulated/fitted and observed values for the Ting-Kirby spiller case. (a) wave height, (b) wave setup, (c)–(i) velocities.  $z/D$  is relative depth.

Note that under the influence of the surface roller, the maximum current speed appears well inside the surfzone. Near the breaking point, the rapid variation of wave heights produces a large momentum gradient, thus drives higher current speeds. To the offshore, the momentum gradient is trivial due to the slowly varying wave heights. Additionally, the horizontal wave turbulent mixing smoothes the cross-shore profile of the current, which will be further discussed in Section 4.3.

Other than the logarithmic form, the observation data indicate that the vertical profile of the longshore currents is near uniform in the surfzone. Hamilton and Ebersole (2001) also found this feature using the LSTF wave flume. An explanation given by Svendsen

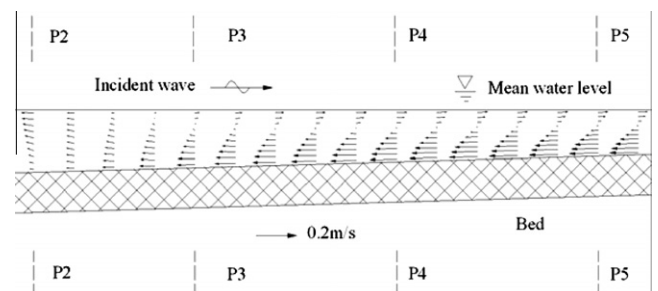


Fig. 3. Period-averaged flow field of the undertow structure for the Ting-Kirby plunger case. The hatched area represents the impermeable bottom.

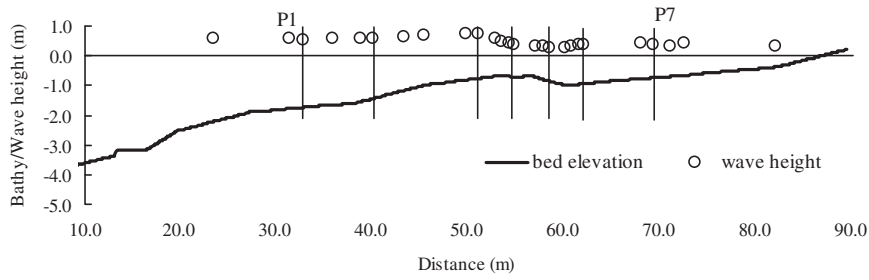


Fig. 4. Bathymetry and measured wave heights of the CROSSTEX wave flume. P1–P7 represent locations of the observation gauges.

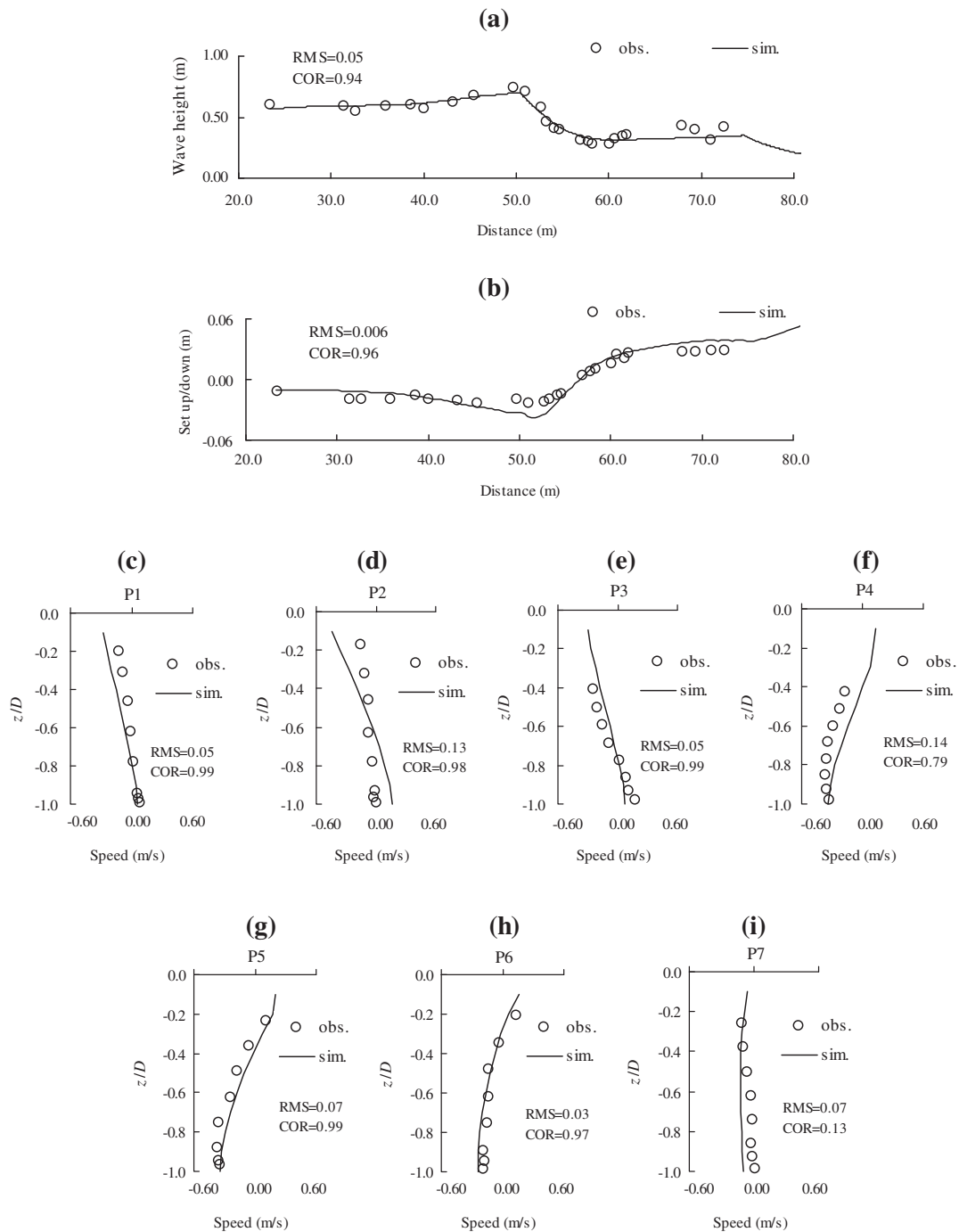
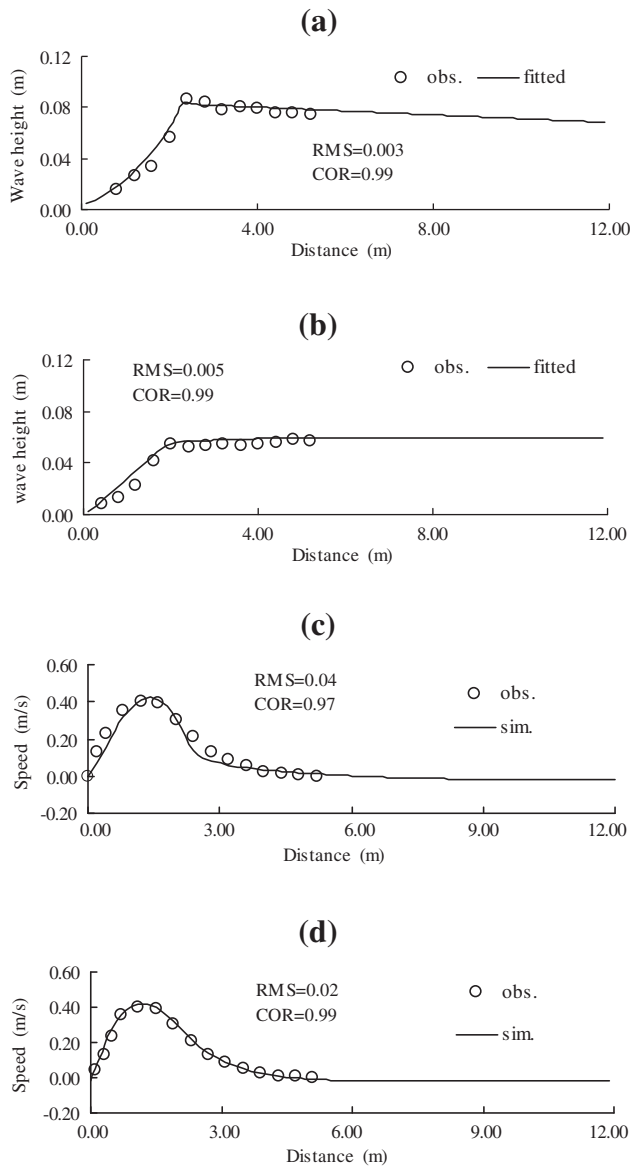


Fig. 5. Comparisons between the simulated and observed values for the CROSSTEX case. (a) wave height, (b) wave setup, (c)–(i) velocities.  $z/D$  is relative depth.



**Fig. 6.** Comparisons between the simulated and observed longshore currents for the Visser cases. (a) wave heights for case 4#; (b) wave heights for case 6#; (c) longshore current speeds for case 4#; (d) longshore current speeds for case 6#.

et al. (2003) is that the wave-induced vertical turbulent mixing would smooth the vertical velocity profile. Detailed discussions on the vertical mixing effect are made in Section 4.4.

Fig. 7 compares the simulated vertical variation of the current with the observed data. The result showed that outside the surfzone, the model is not getting the trends correct (see Fig. 7e to Fig. 7h). To the offshore, the observed speeds at the bottom are even larger than that at the surface. Explanation for this phenomenon is not well reported in the historical literature, and that may be the difference of the wave forcings inside and outside of the surfzone. A more sophisticated theory needs to be developed to solve this.

### 3.3. Rip currents

Borthwick and Foote (2001) have undertaken laboratory studies to investigate the 3D structure of the rip currents over a tri-cuspate beach using the UK Coastal Research Facility (UKCRF). The experimental bathymetry and locations of the observation profiles are

shown in Fig. 8a, where five profiles are arranged in the embayment (P1–P5), and two are arranged on the cusp horn (P6–P7). In this paper, the normal incident case (case B) is used. The incident wave height is 0.125 m, and the wave period is 1.2 s. The input parameters in the numerical model are listed in Table 1.

Waves are simulated using the REF/DIF model. Because the rip current field is complex, and the currents feed back to the wave propagation, thus in the calculation the wave-current interaction must be considered. In this paper, we coupled the REF/DIF program and the hydrodynamic program together through an iterative method. After the current field reaches the stable state, the  $U$  and  $V$  fields are provided to the wave solver, and consequently the new wave parameters are calculated for the preparation of the new residual momentum components. The wave height/direction and current speed data are exchanged in an external transmission file.

Fig. 9 showed the comparison between the simulated and observed wave heights of two representative sections  $y = 14$  m and  $y = 16$  m, where the former is across the embayment, and the latter is across the cusp horn. Due to the complex nature of the wave-current interaction, although the overall distribution features are described ( $RMS = 0.01 \sim 0.02$  m,  $COR = 0.88 \sim 0.97$ ), the modeled wave heights do not rigorously agree with the observed values, with variations in the observed values greater than variations in simulated values.

The flow field of depth-averaged rip currents is illustrated in Fig. 8b, and the comparisons with the observed velocities are shown in Fig. 10. From these figures we notice that a number of symmetric circulation cells develop near the cusps. In the embayment (P1–P5), the currents flow to the offshore with a high speed. Reversely, the currents flow onshore on the horn (P6–P7) with lower speeds.

Theoretically, the  $V$ -velocities should be near-zero because of the symmetric nature of the bathymetry and incident waves. However, the observed  $V$ -velocities are scattered. In fact, in the experiment the rip current has unstable features and a trivial perturbation could lead to a deflection of the current direction. This feature has already been reported in a series of papers. As for the  $U$ -velocities, the  $RMS$  errors are in the range of  $0.03 \sim 0.06$  m/s, and especially the simulated values at sections P6 and P7 are greater than the observed values. One reason is that the gradients of observed wave heights are greater than that simulated in this area, which induces higher speeds (see Fig. 9). The correlations between the two datasets seem not satisfactory compared to other cases, in which the lowest value is  $COR = 0.12$  (section P4). That is because the unstable nature of the rip currents makes the measurement data extremely scattered and their vertical variations are not smooth enough to tell the distribution trends clearly compared to the simulation values. However, through comparisons, the simulated velocity structure of the rip currents captures the major distribution trend.

## 4. Sensitivity analysis

Before simulation of the processes, a number of model parameters should be pre-evaluated. If possible, these parameters should be investigated in situ or through laboratory experiments, but in practice they are usually unavailable. As a result, a calibration process is always mandatory. Therefore, in the following sections we carry out a sensitivity analysis to assess the major model parameters.

### 4.1. Roller energy transfer factor

The roller energy transfer factor  $\alpha$  represents the contribution of the surface roller to the wave-induced stresses, and its value

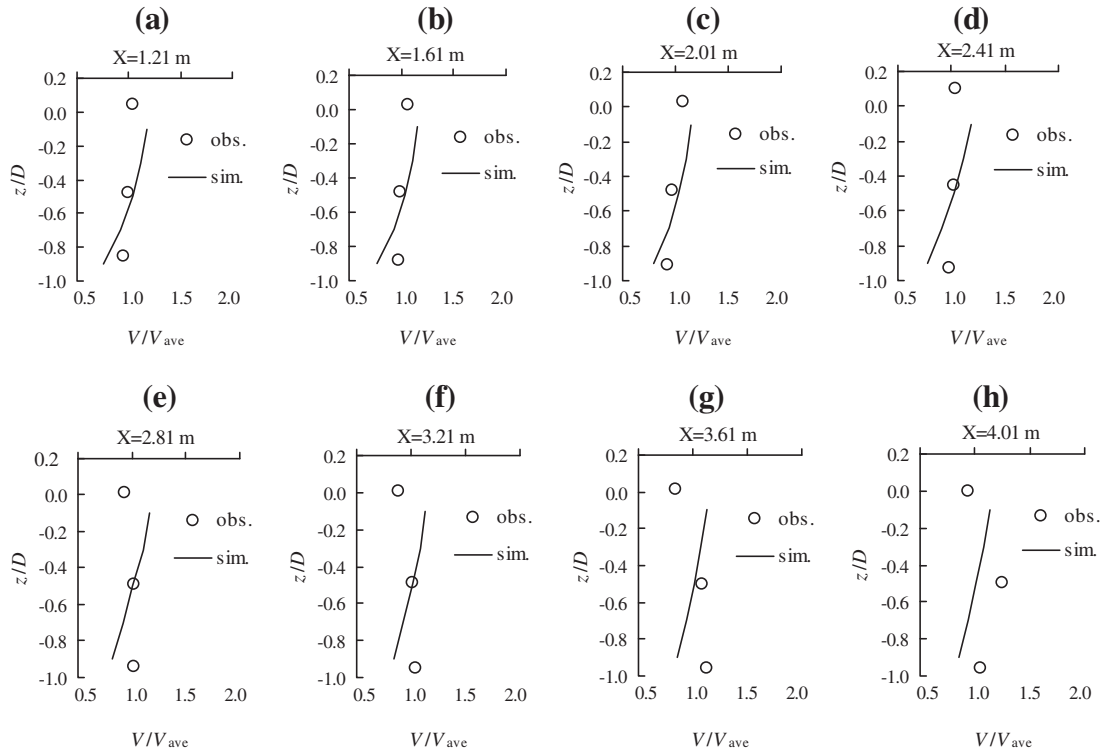


**Fig. 7.** Comparisons between the simulated and observed vertical profiles of the longshore currents for the Visser case 4#. (a)–(h) represent different observation sections.  $z/D$  is relative depth, and  $V/V_{ave}$  is relative velocity.

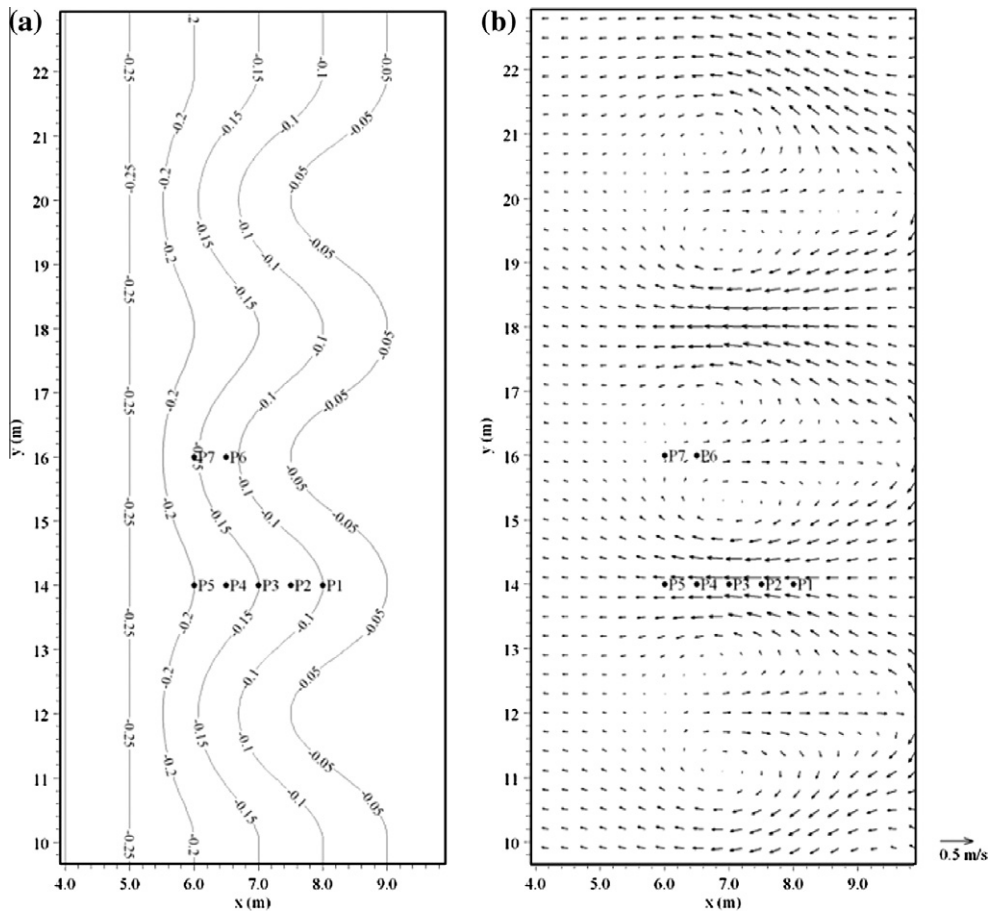


**Fig. 8.** Bathymetry and simulated flow field for the UKCRF experiment. (a) bathymetry; (b) flow field for the depth-averaged speeds.

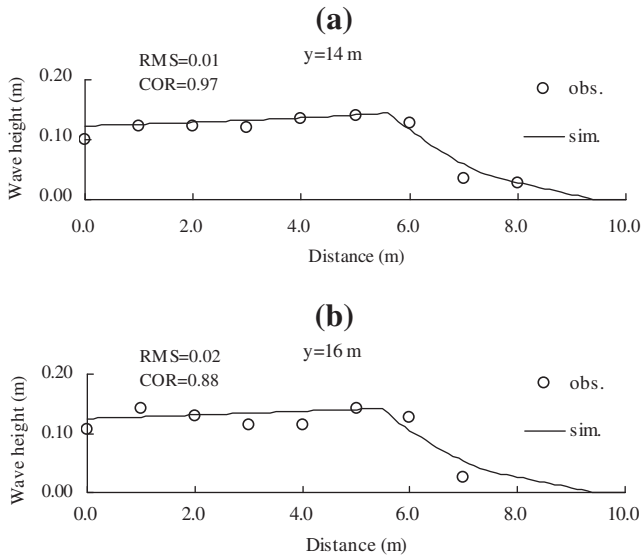


**Fig. 9.** Comparisons between simulated and observed wave heights for the Borthwick and Foote (2001) case. (a) section  $y = 14$  m across the embayment; (b) section  $y = 16$  m across the cusp horn.

should be restricted between 0.0–1.0 (percentage). Taking the Ting–Kirby cases for instance, in Fig. 11 the cross-shore component of the total wave-induced stresses are evaluated, where  $\alpha$  is set at several values varying from 0.0 to 1.0, and the other parameters remain fixed. Theoretically, if the wave breaks, the stresses in the surfzone are formed by two parts: the residual momentum stress  $M_{xx}$  and the roller stress  $R_{xx}$ . Once the wave parameters are specified, the value of  $M_{xx}$  could be calculated explicitly, and could be regarded as constant. But as for  $R_{xx}$ , its value is zero outside the

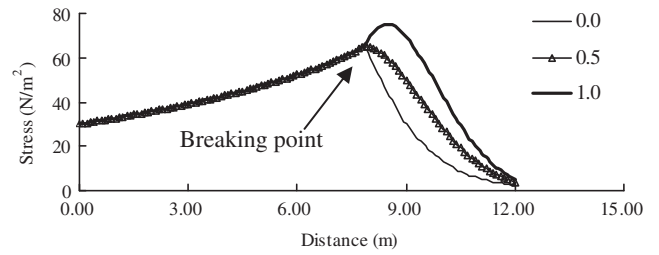


**Fig. 11.** Variations of phase-averaged wave-induced total stress  $M_{xx} + R_{xx}$  under the influence of roller energy transfer factor  $\alpha$ . The Ting and Kirby (1994) case is used for an example.

breaking point, and increases with a larger  $\alpha$  within the surfzone. Fig. 11 indicates that as  $\alpha$  increases, the location of maximum total wave stress  $M_{xx} + R_{xx}$  moves onshore. This conclusion complies with that stated by Svendsen (1984a) and Goda (2006).

Furthermore, the influences of  $\alpha$  to different wave-induced current phenomena are presented in Fig. 12. In the analysis, the CROSSTEX and Visser cases are chosen as examples. The results show that as  $\alpha$  increases, the wave setdown expands towards the shoreline (Fig. 12a), and the peak value of longshore currents shifts toward the shoreline with an increase in the maximum velocity (Fig. 12b).

From Fig. 12c to Fig. 12e, it could be noticed that  $\alpha$  also has impact on the undertow profile. Section P2 (see Fig. 4) is located outside the surfzone, the roller stress  $R_{xx}$  is zero, hence it has no effect on the flow structure. But for sections P4 and P5 within the surfzone, the undertow values become larger as  $\alpha$  increases. The explanation for this effect is that the roller-induced stresses concentrate in the surface layers (see Eq. (17)), firstly the onshore velocity near the surface becomes larger under the impact of the increased stress gradient. Therefore, the undertow near the bottom must increase

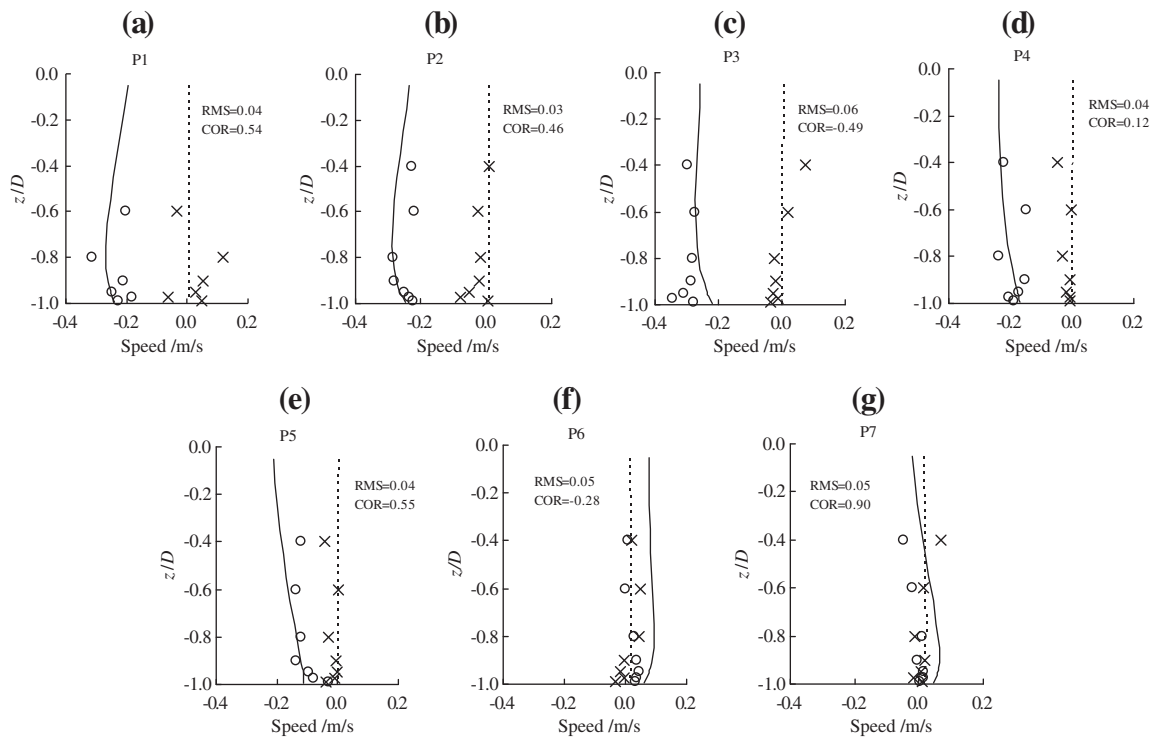


**Fig. 10.** Comparisons between the simulated and observed velocities. Circles represent the observed  $U$ -velocities; crosses mean the observed  $V$ -velocities; and dotted lines mean the simulated  $V$ -velocities. (a)–(g) represent different observation sections.  $z/D$  is relative depth. The error estimations are for the  $U$ -velocities only.

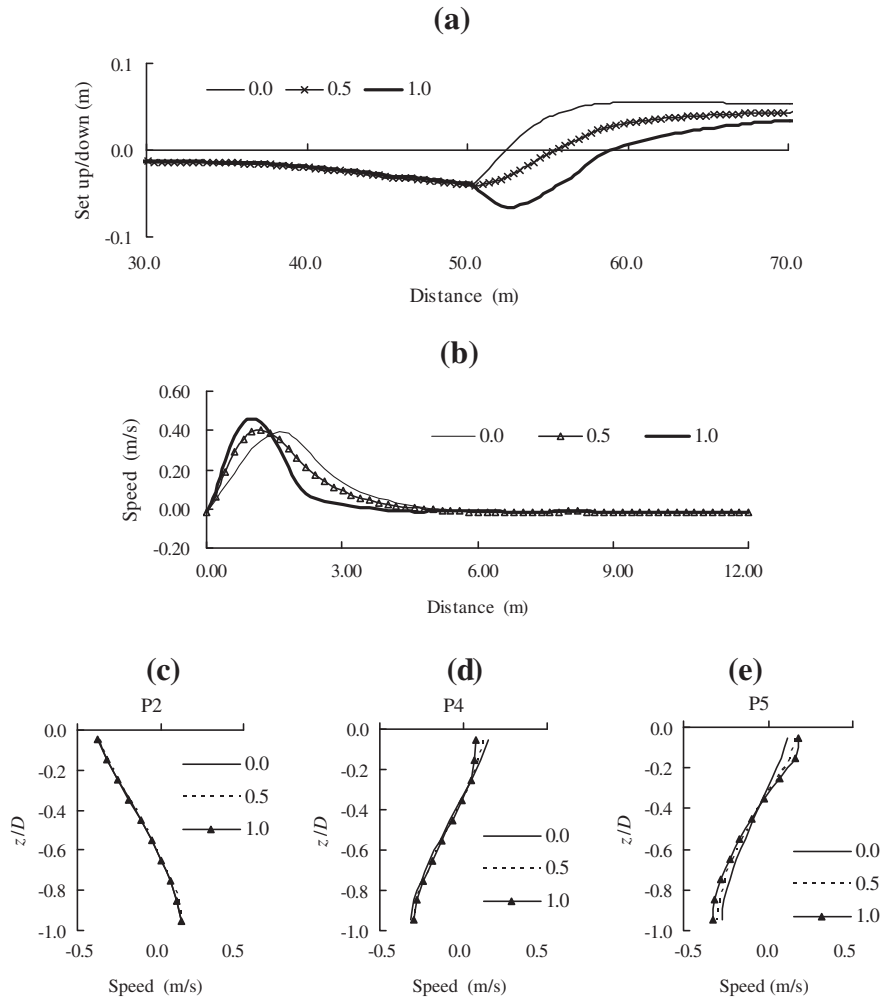


**Fig. 12.** Sensitivity of the roller energy transfer factor  $\alpha$ . (a) wave setup of the CROSSTEX case, (b) longshore current for the Visser 6# case, (c)–(e) velocity profiles for the CROSSTEX case.  $z/D$  is relative depth.

simultaneously to balance the extra surface stresses in order to follow the law that the depth integral should be zero (Lagrangian).

#### 4.2. Roller density

The roller density  $\rho_R$  is another parameter that determines the roller stresses, and in general its value should be less than the seawater density  $\rho$ . However, because the “white capping” over wave crests contains a large amount of air and is extremely turbulent,

and its discontinuous nature makes the description of roller density can only be qualitative, hence  $\rho_R$  is just an empirical parameter. In this sensitivity analysis, the values of  $\rho_R$  varying from  $1000 \text{ kg/m}^3$  to  $600 \text{ kg/m}^3$  are used. Similar to the above discussions on  $\alpha$ , the sensitivity of roller density  $\rho_R$  is demonstrated in Fig. 13 and Fig. 14. The results show that as  $\rho_R$  decreases, the maximum setdown expands onshore, and the peak value of the longshore current increases slightly. Generally, the sensitivity of  $\rho_R$  is smaller than that of  $\alpha$ .

#### 4.3. Horizontal mixing coefficient

The contribution of horizontal turbulent mixing induced by wave motions is evaluated by the variation of coefficient  $\lambda$ . The Visser (1991) cases are used to show its sensitivity, and three values, 0.0, 0.5 and 5.0 are specified. The results are presented in Fig. 15. When  $\lambda = 0.0$ , no wave turbulence is imposed, thus the current speeds are only determined by the gradient of total lateral stress term  $(\partial(M_{xy} + R_{xy})/\partial y)$ . Because the gradient of  $M_{xy} + R_{xy}$  is large near the breaking point and in the surfzone owing to the diffraction, shoaling and breaking processes of the wave propagation, thus the current speeds are greater in these areas. Conversely, outside the surfzone  $\partial M_{xy}/\partial y \approx 0$ , and no roller effect is imposed, thus the longshore current speeds are small. The turbulent mixing

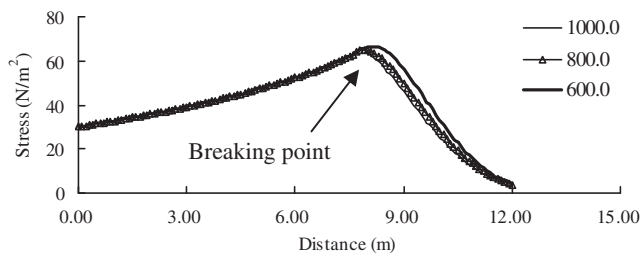


**Fig. 13.** Variations of phase-averaged wave-induced total stresses under the influence of the roller density  $\rho_R$ . The Ting and Kirby (1994) case is used for an example.

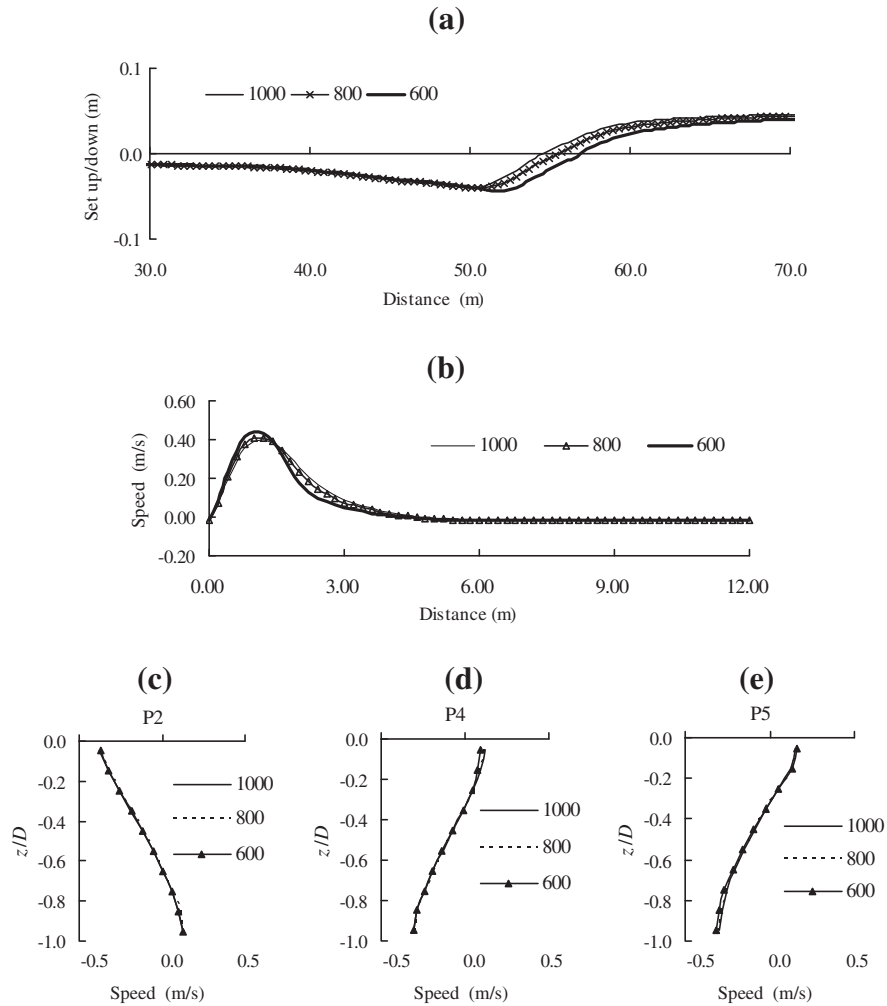


**Fig. 14.** Sensitivity of the roller density  $\rho_R$ . (a) wave set-up of CROSSTEX case; (b) longshore currents for Visser 6# case; (c)–(e) velocity profiles for the CROSSTEX case.  $z/D$  is relative depth.

becomes more significant as  $\lambda$  increases. That is, the cross-shore profile of current speeds is smoothed and the peak value reduced.

If  $\lambda = 5.0$ , the cross-shore variation of the current speed is greatly reduced. This effect agrees with that stated by Goda (2006).

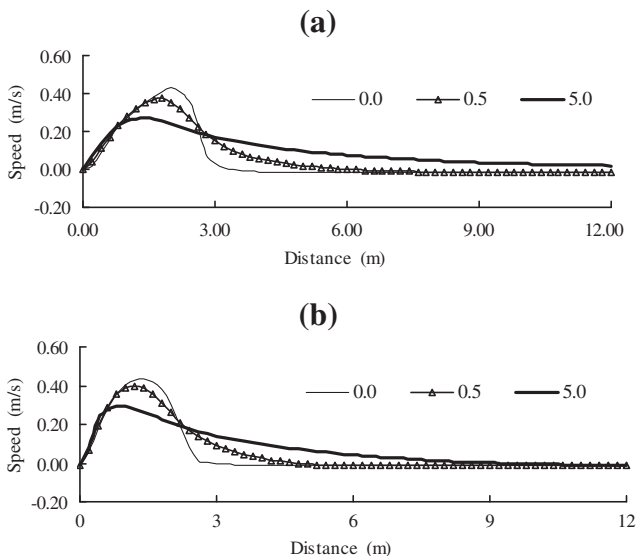


**Fig. 15.** Sensitivity of the wave horizontal turbulent mixing coefficient  $\lambda$ . (a) Longshore currents for the Visser case 4#; (b) longshore currents for the Visser case 6#.

#### 4.4. Vertical mixing coefficient

In Eq. (13), a calibration parameter  $b$  is introduced to account for vertical turbulent mixing. Through sediment flume experiments, Wang (1984) recommended  $b = 0.0025$ . The CROSSTEX experiment is used to analyze its sensitivity, and three values of 0.01, 0.001 and 0.0001 are specified. The results are shown in Fig. 16.

Note that as  $b$  increases, the enhanced mixing weakens the vertical circulation structure of the undertow. When  $b$  is set to 0.01, the speeds are nearly uniform along the profile. This means the wave vertical turbulent mixing coefficient  $b$  is a sensitive parameter in the model, especially for the modeling of vertical structure. Therefore, it should be evaluated carefully in the calibration processes.

#### 4.5. Discussions

When the wave breaks, the significant nonlinearity means that the vertical distribution of residual momentum does not strictly follow the expression in Eq. (5). Additionally, other than the sinusoidal form, the shape of the breaking waves is more close to the Cnoidal type. Therefore, the formulations derived under linear

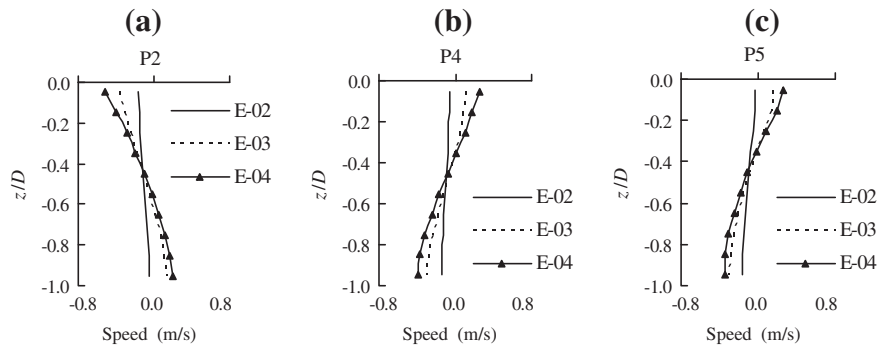


Fig. 16. Sensitivity of the wave vertical turbulent mixing coefficient  $b$ . (a)–(c) represent different observation sections of the CROSSTEX case.  $z/D$  is relative depth.

wave theories contain inevitable errors compared to the realistic situations. This reminds us in the modeling of the wave-induced nearshore currents, the calibration parameters should not be determined under any individual case, but be deliberately analyzed against plenty of cases. Only by this approach, the generality of the numerical model could be best ensured.

In this paper, the major controlling calibration parameters consist of the roller energy transfer factor  $\alpha$ , roller density  $\rho_R$ , wave horizontal turbulent mixing coefficient  $\lambda$  and vertical mixing coefficient  $b$ . Owing to the complexity of the surface roller itself, the relevant parameters describing the roller could only be empirical and qualitative. Nevertheless, the physical background of  $\alpha$  and  $\rho_R$  is explicit, where  $\alpha$  has the meaning of “percentage”, thus its value must be confined in the range of 0.0 to 1.0, and  $\rho_R$  must be less than the seawater density because it contains air. According to the analysis for these two parameters,  $\alpha$  is more sensitive compared to  $\rho_R$ , and its range falls in 0.3 to 0.6. A value varying from 800 kg/m<sup>3</sup> to 900 kg/m<sup>3</sup> seems appropriate for  $\rho_R$  through the validations in this paper.

The value of wave vertical turbulent mixing coefficient  $b$  strongly affects the modeling precision of undertow. However, the physical background of parameter  $b$  is not sound, and must be evaluated through a tuning process. If we calibrate  $b$  using different cases separately, the ultimate values even are not in the same order. For example, in the Visser (1991) experiments, the vertical profile of longshore current within the surfzone is uniform, especially the speed gradient is approximately unity near the breaking point (see the  $X = 1.61$  m section in Fig. 7). If we set  $b = 0.01$ , the vertical profiles could be better fitted. However, a same  $b$  value almost smears the undertow structures (see Fig. 16). That brings in a contradiction for the selection of parameter  $b$ . Through comparisons amongst all cases used in this paper, although it could not fit all the vertical current profiles satisfactorily, a compromising  $b = 0.001$  seems reasonable, and this value is in the same order with that recommended ( $b = 0.0025$ ) by Wang (1984).

Wave horizontal turbulent mixing coefficient  $\lambda$  is another important parameter controlling the planar layout of current speeds, and an inappropriate value could induce a too sharp or smooth current field if is not well argued. According to inter-comparisons, a range of 0.2 to 0.5 seems reasonable, and this range is close to that suggested by Goda (2006).

Table 2

Recommended ranges of the major calibration parameters in the established 3D wave-induced current model.

Model parameter	$\alpha$	$\rho_R$	$b$	$\lambda$
Range	0.30 ~ 0.60	800 kg/m <sup>3</sup> ~ 900 kg/m <sup>3</sup>	0.001	0.20 ~ 0.50

In table 2 the ranges of major calibration parameters in the validation processes are listed, which could be used as a reference for coastal modelers. Note that the ranges for parameters are similar to those reported in historical papers, and this consistency further validates the model in another aspect. However, it should be stressed that these parameter ranges are only calibrated from numerical simulations, hence their values are empirical. If the precise value of a specified parameter is the main interest, a physical model using a single-factor analysis is suggested.

## 5. Conclusions

- (1) A three-dimensional hydrodynamic model for the simulation of wave-induced nearshore currents is established. The wave-induced depth-varying residual momentum, surface roller evolution, wave turbulent mixings are incorporated in the model as the major driving forces. The wave-current interacted bottom shear stresses are also taken into consideration.
- (2) A surface roller evolution model is developed considering the roller energy transfer, roller density and the bottom slope dissipation. The expression of the wave-induced horizontal turbulent mixing coefficient proposed by Larson and Kraus (1991) is extended to the three dimensional form.
- (3) Several experimental cases are utilized to validate the established model. The cases cover a variety of wave-induced current phenomena including the wave setup (1D), undertow (2DV), longshore currents (quasi-3D) and rip currents (3D). The validation results showed the model could effectively grasp their major features, and perform reasonably for most of the cases.
- (4) Surface rollers should be considered in the modeling of the wave-induced currents inside the surfzone. Incorporation of the roller evolution model could effectively explain the shoreward shift of the maximum wave setdown and the peak longshore current speed. The wave-induced turbulent mixing effect contributes to the distribution of current velocity in both horizontal and vertical directions.
- (5) Through sensitivity analysis, the recommended ranges of the major calibration parameters are: surface roller energy transfer factor  $\alpha \in (0.3, 0.6)$ , surface roller density  $\rho_R \in (800, 900)$  kg/m<sup>3</sup>, wave vertical turbulent mixing coefficient  $b \approx 0.001$ , wave horizontal turbulent mixing coefficient  $\lambda \in (0.2, 0.5)$ .

## Acknowledgements

Sincere thanks are addressed to Prof. Zhang Wei and Dr. Zhang Chi from Hohai University, China and Prof. Li Shao-wu from Tianjin

University, China for their guidance and comments on this manuscript. Dr. Zhang Yifeng helped a lot on the wave modelling. This work is funded by the Central Public Institute Foundation of Tianjin Research Institute for Water Transport Engineering, M.O.T., (Grant No. TKS100102). The comments provided by the anonymous reviewers have greatly enhanced the manuscript, and thanks must be addressed to them as well.

## References

- Ardhuin, F., Rasche, N., Belibassakis, K.A., 2008. Explicit wave-averaged primitive equations using a generalized Lagrangian mean. *Ocean Modelling* 20, 35–60.
- Battjes, J.A., 1975. Modelling of turbulence in the surfzone. *Proc. Symp. Modeling Techniques*, 1050–1061.
- Borthwick, A.G.L., Foote, Y.L.M., 2001. Wave-induced currents at a tri-cusped beach in the UKCRF. *Water and Maritime Engineering* 154 (4), 251–263.
- Dally, W.R., Brown, C.A., 1995. A modeling investigation of the breaking wave roller with application to cross-shore currents. *Journal of Geophysical Research* 100 (C12), 24,873–24,883.
- Duncan, J.H., 1981. An experimental investigation of breaking waves produced by a towed hydrofoil. *Proceedings of the Royal Society of London Series, A* 377, 331–348.
- Engelund, F., 1981. A simple theory of weak hydraulic jumps. In *Prog. Rep. 54, Inst. of Hydrodyn. and Hydraul. Eng. (ISVA)*. Tech. Univ. of Denmark, Horsholm, 29–32.
- Goda, Y., 2006. Examination of the influence of several factors on longshore current computation with random waves. *Coastal Engineering* 53, 157–170.
- Haas, K.A., Warner, J.C., 2009. Comparing a quasi-3D to a full 3D nearshore circulation model: SHORECIRC and ROMS. *Ocean Modelling* 26, 91–103.
- Hamilton, D.G., Ebersole, B.A., 2001. Establishing uniform longshore currents in a large-scale sediment transport facility. *Coastal Engineering* 43, 199–218.
- Kirby, J.T., Dalrymple, R.A., Shi, F.Y., 1994. REF/DIF 1 Version 2.5 Center for Applied Coastal Research. CACR Report No. 94–22.
- Larson, M., Kraus, N.C., 1991. Numerical model of longshore current for bar and trough beaches. *Journal of Waterway, Port, Coastal and Ocean Engineering* 117 (4), 326–347.
- Lin, P. Z., Zhang, D., 2004. The depth-dependent radiation stresses and their effect on coastal currents. *Proceedings of the 6th International Conference of Hydrodynamics: Hydrodynamics VI Theory and Applications*, pp.247–253.
- Longuet-Higgins, M.S., Stewart, R.W., 1964. Radiation stress in water waves: a physical discussion with applications. *Deep Sea Research*, 11, 529–562.
- McWilliams, J.C., Restrepo, J.M., Lane, E.M., 2004. An asymptotic theory for the interaction of waves and currents in coastal waters. *Journal of Fluid Mechanics* 511, 135–178.
- Mellor, G.L., Yamada, T., 1982. Development of a turbulence closure model for geophysical fluid problems. *Review of Geophysics and Space Physics* 20 (4), 851–875.
- Mellor, G.L., 2003. The three-dimensional current and surface wave equations. *Journal of Physical Oceanography* 35, 2291–2298.
- Mellor, G.L., 2005. Some consequences of the three dimensional current and surface wave equations. *Journal of Physical Oceanography* 33, 1978–1989.
- Oey, L.Y., 2006. An OCGM with movable land-sea boundaries. *Ocean Modelling* 13, 176–195.
- Okayasu, A., Shibayama, T., Mimura, N., 1990. Velocity field under plunging waves. *Proc. Coastal Engineering Conf.*, 22: 68–81.
- Putrevu, U., Svendsen, I.A., 1999. Three-dimensional dispersion of momentum in wave-induced nearshore currents. *European Journal of Mechanics-B/Fluids* 18 (3), 409–427.
- Scott, C.P., Cox, D.T., Shin, S., Clayton, N., 2004. Estimates of surf zone turbulence in a large scale laboratory flume. In *proceedings of the 29th International Conference of Coastal Engineering*.
- Smagorinsky, J.S., 1963. General circulation experiments with the primitive equations- I, the basic experiment. *Monthly Weather Review* 91, 99–164.
- Soulsby, R.L., Hamm, L., Klopman, G., Myrhaug, D., Simons, R.R., Thomas, G.P., 1993. Wave-current interaction within and outside the bottom boundary layer. *Coastal Engineering* 21, 41–69.
- Svendsen, I.A., 1984a. Wave heights and set-up in a surf zone. *Coastal Engineering* 8, 303–329.
- Svendsen, I.A., 1984b. Mass flux and undertow in a surf zone. *Coastal Engineering* 8, 347–365.
- Svendsen, I.A., Qin, W., Ebersole, B.A., 2003. Modelling waves and currents at the LSTF and other laboratory facilities. *Coastal Engineering* 50, 19–45.
- Swart, D.H., 1974. Offshore sediment transport and equilibrium beach profiles. *Delft Hydraulics Lab., Publ.*, 131.
- Tajima, Y., Madsen, O.S., 2002. Shoaling, breaking and broken wave characteristic. In *Proceedings of the 28th Conf. World Scientific, Cardiff, Wales*, pp. 222–234.
- Ting, F.C.K., Kirby, J.T., 1994. Observation of undertow and turbulence in a laboratory surf zone. *Coastal Engineering* 24, 51–80.
- Visser, P.J., 1991. Laboratory measurements of uniform longshore currents. *Coastal Engineering* 15, 563–593.
- Wang, B., Andrew, A.J., Otta, A.H., 2008. Derivation and application of new equations for radiation stress and volume flux. *Coastal Engineering* 55, 302–318.
- Wang, S.Y., 1984. Vertical distribution of suspended sediment concentration under wave action. *Science in China Series A, Mathematics, Physics, Astronomy, & Technological Science*. 12, 1151–1160. (in Chinese).
- Warner, J.C., Sherwood, C.R., Signell, R.P., Harris, C.K., Arango, H.G., 2008. Development of a three-dimensional, regional, coupled wave, current, and sediment-transport model. *Computers and Geosciences* 34, 1284–1306.
- Wu, X.Z., Zhang, Q.H., 2009. A three-dimensional nearshore hydrodynamic model with depth-dependent radiation stresses. *China Ocean Engineering* 23 (2), 291–302.
- Xia, H.Y., Xia, Z.W., Zhu, L.S., 2004. Vertical variation in radiation stress and wave-induced current. *Coastal Engineering* 51, 309–321.
- Xie, L., Liu, H., Peng, M., 2008. The effect of wave-current interactions on the storm surge and inundation in Charleston Harbor during Hurricane Hugo 1989. *Ocean Modelling* 20, 252–269.